



## Conditional summertime day-ahead solar irradiance forecast

John F. Mejia<sup>a,\*</sup>, Marco Giordano<sup>b</sup>, Eric Wilcox<sup>a</sup>

<sup>a</sup> Department of Atmospheric Sciences, Desert Research Institute (DRI), USA

<sup>b</sup> Atmospheric Sciences Graduate Program, University of Nevada-Reno, Department of Atmospheric Sciences, DRI, USA



### ARTICLE INFO

#### Keywords:

Model Output Statistics  
Global horizontal irradiance  
Moisture surges  
North American Monsoon  
Numerical Weather Prediction

### ABSTRACT

We investigated the accuracy of numerical weather prediction (NWP)-based global horizontal irradiance (GHI) and clear-sky index forecasting over southern Nevada. Accurate forecasts of solar irradiance are required for electric utilities to economically integrate substantial amounts of solar power into their power generation portfolios. Solar irradiance forecasting can enhance the value of renewable energy by anticipating fluctuations in these variable resources. Summertime cloud variability depends largely on the combination of tropical and extratropical synoptic-scale forcing, most of which is observable, predictable, and highly related to the North American Monsoon moisture surge events. We used high-resolution realtime NWP output based on the weather and research forecasting (WRF) model to study the ability of the model to deliver day-ahead GHI and clear-sky index forecasts for a the National Renewable Energy Laboratory (NREL)-University of Nevada site, located in Las Vegas, Nevada. High-resolution forecast products were obtained from the Desert Research Institute (DRI) archived real-time numerical weather forecasting products. Results showed the importance of developing a site-specific seasonal and weather-dependent model output statistics (MOS) approach to improving forecast accuracy, which removes the bias and reduces the overall relative root-mean – square error (rRMSE) of GHI by as much as 6%, when compared to the uncorrected model output; improving forecast accuracy is obtained by adding information that relates regional-scale circulation patterns driving cloudiness, hence irradiance variability to the target area. We show the seasonal dependence of the NWP forecast accuracy and demonstrate that intelligent weather functions provide a pathway to improve accuracy of solar forecasts further.

### 1. Introduction

Current solar forecasting technologies use a mixture of tools to improve the forecast, ranging from statistical data approaches to physically-based deterministic and probabilistic models. Optimizing the implementation of these tools to increase forecast accuracy can reduce costs and increase the reliability of integrating solar power into the electricity grid (Lorenz et al., 2009).

Numerical weather prediction (NWP) models are physically based and generally the most accurate tool for solar global horizontal irradiance (GHI) forecasting for forecast windows lasting hours to several days (Perez et al., 2013; Mathiesen and Kleissl, 2011; Jimenez et al., 2016). Improved forecasting requires high quality and reliable real-time data from widespread networks of upper-air and ground-based instruments. These data define the model's initial conditions using data assimilation tools. Today, state-of-the-art, high-resolution NWP models are capable of resolving clouds (stratiform and convective), fog-filling valleys, orographic precipitation, and even local processes related to the urban heat island effect. NWP systems such as NOAA's High-

Resolution Rapid Refresh (NOAA-HRRR; Benjamin et al., 2004), the Advanced Research-Weather and Research Forecasting model (WRF; Skamarock et al., 2008), among other models, are becoming essential tools to provide critical information for various weather-related sectors, including the energy industry. Nevertheless, stubborn sources of uncertainty – because of imperfections in parameterization of the model's physics, chaotic behavior of the weather, complex topography, imperfect initial conditions, among other challenges – persist in NWP systems, leading to model imperfections. Quantifying the model's errors, systematic and random, is then a necessary task to assess whether its output is suitable to guide resource-management decisions.

Forecast post-processing approaches called model output statistics (MOS) can improve NWP model forecasts (Perez et al., 2013) and have proved to be more useful in correcting systematic biases (Perez et al., 2013; Zhang et al., 2013a,b; Sengupta et al., 2015). MOS approaches implement statistical regressions ranging from linear regression methods to sophisticated machine-learning tools designed to perform deeper error structure and pattern recognition for more intelligent NWP output correction (Sharma et al., 2011; Lauret et al., 2014; Alessandrini

\* Corresponding author.

E-mail address: [john.mejia@dri.edu](mailto:john.mejia@dri.edu) (J.F. Mejia).

et al., 2015). In general, all MOS approaches seek to optimize NWP model output by relating locally or regionally observed parameters to site-specific conditions (Badosa et al., 2015). Bias correction approaches are often implemented without careful consideration of the source of the bias (a challenging task), however, and without considering regional or local physical processes responsible for cloudiness variations in the region. Differentiating between error sources can be important to selectively correct forecasts and create more accurate MOS tools (Lauret et al., 2014).

Mejia et al. (2016) showed that cloudiness over the U.S. Southwest – including New Mexico, Arizona, and southern Nevada – is related to North American Monsoon (NAM; Adams and Comrie, 1997) synoptic-scale wet spells called “moisture surges.” Moisture surges are observable and predictable weather patterns in the NAM region and are modulated by different tropical and extratropical synoptic-scale features – including inverted troughs, tropical easterly waves, eastern Pacific tropical storms, tropical cyclones, and extratropical waves (Higgins and Shi, 2001; Seastrand et al., 2014; Mejia et al., 2016). These features predominantly occur during July–September and then tend to increase monsoonal moisture transport through the Gulf of California – reaching northwestern Mexico and the southwestern U.S. and increasing moisture instability – leading to increased storminess and organized convection in the region. We argue that this cloudiness drives variability of solar resources in the southwestern US during the NAM.

Kim and Clarkson (2016) developed a study to improve GHI and direct normal irradiance using an NWP model based on the WRF (with aerosol interaction) over Arizona and showed that the model performed poorly during the 2011 NAM season, likely related to the frequent but variable nature of clouds during the 2011 NAM season. Here we argue that forecast improvement for hours to day-ahead time windows can be improved by conditioning the forecast products by developing a process-based MOS that considers NAM moisture-surge episodes.

We focused on performing a detailed forecast accuracy assessment of day-ahead GHI and clear-sky index ( $Kt^*$ ) using real-time forecast output from the NWP model based on the WRF. Specifically, we present forecast comparisons against GHI observations from a site in Las Vegas, Nevada. The accuracy assessment implements multiple forecast error metrics that enable us to quantify the benefit and sensitivity of implementing different MOS approaches and training techniques. Specifically, the training technique determines parameter and site (or region) specific bias correction quantities associated with composite events characterized by canonical relative humidity state and regional-scale flow regimes referred to as weather functions in this study.

## 2. Data and methodology

### 2.1. Evaluation observations

We used GHI surface observations from a National Renewable Energy Laboratory (NREL)-University of Nevada, Las Vegas site (NREL-UNLV; Andreas and Stoffel, 2006; 36.06° N, 115.08° W, 615 m ASL). The station provides observations at 1-min. time increments, aggregated and synchronized using 1-h time increments to match the model output. Of note is that observations were not categorized by changes in GHI because of haze, smoke, or dust – which can be an important source of GHI variations (~10%; Zack, 2010) in the Las Vegas region (Chow et al., 1999) and can impact model evaluation procedures.

### 2.2. Clear sky index

A common parameter derived from GHI is the clear sky index ( $Kt^*$ ). The  $Kt^*$  is defined as the ratio of irradiance to irradiance during clear sky conditions at any given time ( $GHI_{clear}$ ).  $Kt^*$  normalizes GHI between 0 and 1 (for clear sky conditions), reducing the potential of introducing non-stationarities into the statistical approaches from the irradiance

diurnal cycle and seasonality (Voyant et al., 2015). In this study and for simplicity, we estimated the  $GHI_{clear}$  using the Ineichen and Perez clear sky model with climatology parameters for the state of the atmosphere (Ineichen and Perez, 2002; Reno et al., 2012) and using Holmgren and Groenendyk (2016) procedures.

### 2.3. High-resolution NWP model

We implemented archived weather forecast data from the Desert Research Institute (DRI) operational weather forecast system starting August 1, 2015 and continuing to December 31, 2016. DRI performs real-time, fine-resolution NWP simulations based on the Weather and Research Forecasting model (WRF; Skamarock and Klemp, 2008; Skamarock et al., 2008). The model domains are 18 km over the western U.S., 6 km-nested domains covering California and Nevada, and two nested domains at 2 km independently covering the Reno-Tahoe and Las Vegas urban and suburban areas (Fig. 1).

The WRF configuration follows physics and integration strategies shown in Dorman et al. (2013), with some modifications and different domain-grid configuration outlined below. We designed the selection of model setup through basic and common knowledge of the prevailing physical processes that dominate regional climate variations over the western U.S. (Leung et al., 2003; Rasmussen et al., 2011; Liou et al., 2013; Silverman et al., 2013; Zhang et al., 2013a,b; Dorman et al., 2013). A summary of the WRF model main configuration and parameters is presented in Table 1. It is well known, however, that the selection of optimal parameters and physics configuration for WRF is a challenging task depending on many factors, including the following: initial/boundary conditions, regional climate and its variability, and simulation grid size (Liang et al., 2012; Diagne et al., 2014; Fernández-González et al., 2015). Controlling all these factors and all the parameters involved in the WRF as a real-time forecasting tool is outside the scope of this report, requiring time and resources not available for this study. The WRF is driven by initial and lateral boundary conditions provided by Global Forecast Systems (GFS; <http://www.emc.ncep.noaa.gov/GFS/doc.php>), while integrating the dynamic equations and physics parameterizations at the interior grids at finer spatial and temporal scales. GFS is produced and periodically updated by the National Centers for Environmental Prediction (NCEP). The horizontal grid spacing for GFS data is 0.25 arc degree with 32 vertical layers, including lateral boundary conditions of surface, atmosphere, and soil variables every three hours. The GFS data assimilation system was updated in May 2016 to include a dual-resolution hybrid four-dimensional ensemble-variational assimilation system intended to improve the model's initialization and forecast accuracy. At the time of this study, we were not aware of any studies and showing evidence of any improvements in the GFS system. Note that these GFS changes could have introduced some systematic differences and trends in the forecast error structure of this study. Our relatively short period of simulated records prevents us from examining and accounting for such potential differences. In this study, we assumed that such differences were small and to the best of our knowledge, there are no published results indicating that this assumption precludes our methodological approach and assessment.

Zempila et al. (2016) and Ruiz-Arias et al. (2013) found that the Dudhia scheme performs adequately under clear-sky conditions. If aerosols are considered, however, Ruiz-Arias et al. (2013) suggested that the RRTMg (a different shortwave parameterization approach implemented within the WRF) tends to perform better than the Dudhia scheme. The NWP systems described above does not consider aerosol interactions with clouds and radiative processes, which could be important drivers of solar irradiance variability (on the order of 10%) in the southwestern U.S. (Kim and Clarkson, 2016).

Real-time forecast products were produced twice per day (00 and 12 UTC). For this study, the model GHI and other ancillary forecast parameters were retrieved using the nearest grid point to the NREL-UNLV site. Day-ahead hourly GHI forecasts were archived consistently

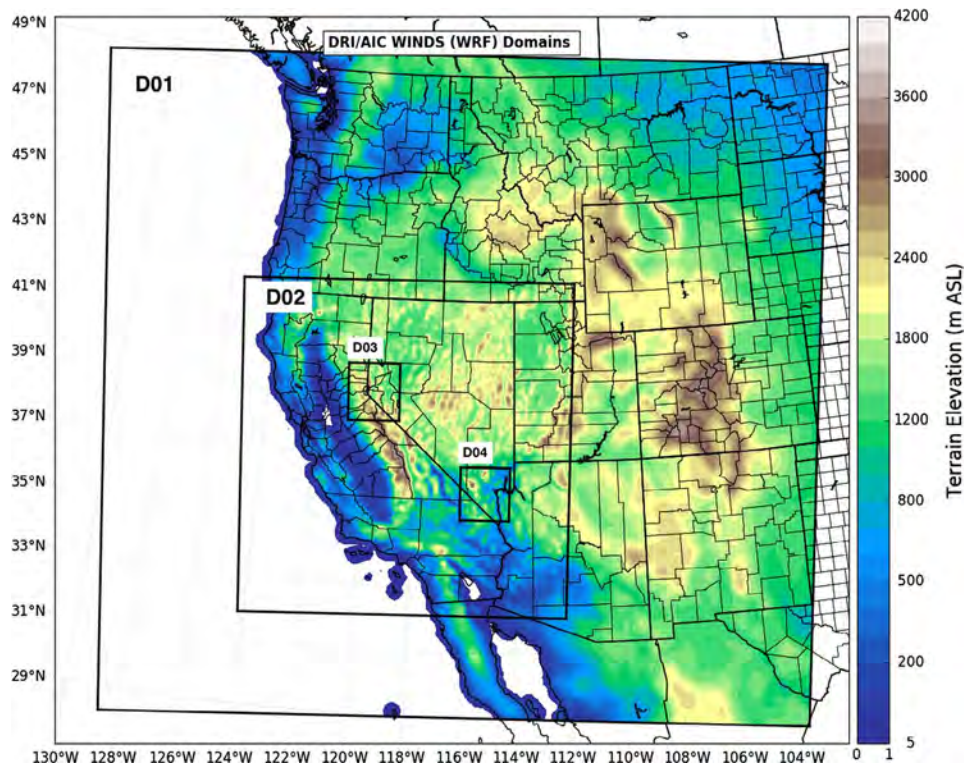


Fig. 1. DRI-RCM model nested domains using D01 = 18 km, D02 = 6 km, and D03 and D04 = 2 km (grid sizes). Shaded contours correspond to the terrain elevation using each simulated domain resolution. D04 is centered around Las Vegas.

since Aug. 2015. One note is that a day-ahead forecast for the 12 UTC forecasts provides only a two-to-three hour spin-up before daylight, which can have a negative impact in the model’s representation of the physics of clouds, thereby affecting radiation processes. Of note is that the night values were excluded. To add fairness and realism in the timing of the cloudy episodes, AM and PM values were treated separately regardless of the MOS scenarios and approaches.

2.4. MOS training scenarios and approaches

Our main foci were to perform an accuracy assessment of the model’s performance and investigate the impact of different MOS approaches and training techniques (hereafter, “scenarios”) that incorporated observable and predictable local/regional processes that correlated well with cloud variability in the Las Vegas area.

Traditional MOS approaches use fixed seasonal (stationary) bias correction predictor/predictant relationships (Glahn and Lowry, 1972; Jacks et al. 1990; Roebber, 2010; Cui et al., 2012), which assume stationarity and do not account for intraseasonal-to-interannual variations or early/delay onset of seasonal transitions. The post-processing approaches adopted here are designed for a specific site and use the simulated target parameter and corresponding local observations at a desired site.

2.4.1. MOS scenarios

2.4.1.1. Seasonally adjusted MOS. A novel aspect of our MOS approach is the use of a simple optimization of the bias correction of model output using bootstrapping, which is accomplished by dividing the historical forecast into two periods – a training and a validation period. The former was used for estimating the parameters by minimizing the bias and root-mean-square error (RMSE). We used seasonal training

Table 1 Model setting for WRF used at the Desert Research Institute.

Domain/Integration settings	Domain 1 18 km grid size	Domain 2 6 km grid size	Domain 3 2 km grid size	Domain 4 2 km grid size
Horizontal and vertical grid cells	140 × 130 × 65	193 × 196 × 65	101 × 100 × 65	101 × 100 × 65
Slope radiation	On	On	On	On
Topographic shading	On	On	On	On
Downscaling	One-way	One-way	One-way	One-way
Output time increments	Hourly	10 min	10 min	10 min
Time step (maximum)	90 s	30 s	10 s	10 s
<i>Physics parameterizations</i>				
Boundary layer	MYJ-TKE (Janjic, 1994)	MYJ-TKE (Janjic, 1994)	MYJ-TKE (Janjic, 1994)	MYJ-TKE (Janjic, 1994)
Cumulus	K&F	Explicit	Explicit	Explicit
Microphysics	Thompson (Thompson et al., 2008)			
Land surface model	Noah Multi-Physics (Niu et al., 2011)	Noah Multi-Physics- (Niu et al., 2011)	Noah Multi-Physics- (Niu et al., 2011)	Noah Multi-Physics- (Niu et al., 2011)
Radiation (shortwave and longwave)	Dudhia (Dudhia, 1989) and RRTM (Mlawer et al., 1997)	Dudhia (Dudhia, 1989) and RRTM (Mlawer et al., 1997)	Dudhia (Dudhia, 1989) and RRTM (Mlawer et al., 1997)	Dudhia (Dudhia, 1989) and RRTM (Mlawer et al., 1997)

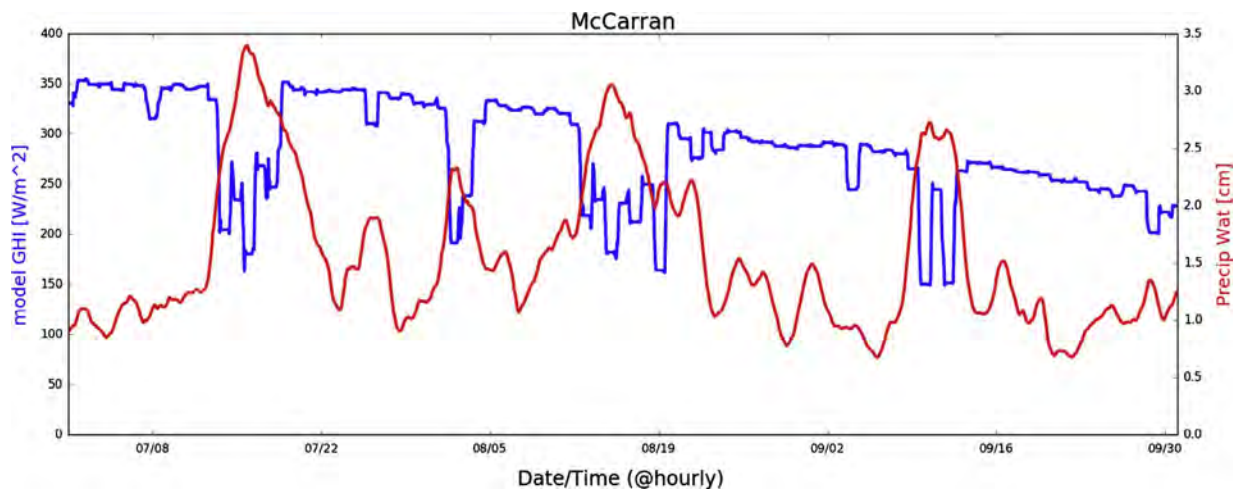


Fig. 2. NREL/NSRDB 24-h moving average of modeled GHI (MM/DD) and Precipitable Water at McCarran site (Las Vegas) during NAM-2004 (Wilcox, 2007). Note that peaks in PW are related to significant decreases in global radiation. Also of note is that all relatively high values in PW are related to well-documented 2004 surge events, July 12–15, Aug 2–4, and Sept 10–13 (Mejia et al., 2010; Johnson et al., 2007).

windows longer than 90 days to increase the likelihood of including similar weather functions and retain the range of variability, making the approach suitable for extreme events. Also, the longer the training period, the larger the number of independent samples in the training data. Systematic errors, however, may potentially vary from one synoptic event to the next. Alternatively, a very long training period (> 120 days) would cross seasonal transitions, increasing uncertainty because of marked seasonal dependencies in the error structure (Akarslan and Hocaoglu, 2016). Training periods from similar seasons using multiyear data sets would be helpful but are typically inadequate due to non-stationarities related to inter-annual climate variations. Moreover, maintaining long historical forecast data sets (multiyear) is expensive and often contains inadequate/inhomogeneous samples because of: (i) changes to the global model used as the boundary condition; (ii) global/regional/mesoscale models are constantly undergoing upgrades; (iii) increases in model resolution that accompany steady improvements in computing efficiency. If the systematic errors in the simulated output are consistent, then 45–120 day training data sets may be adequate for correction of systematic forecast errors, while controlling the stationarity assumption of the regressions analysis or correction functions.

**2.4.1.2. Relative humidity at the surface (Weather Function 1 or WxF1).** Moist processes and convective cloud parameterization and microphysics are perhaps the most challenging processes in NWP modeling systems. In arid climates, cold moist environments have been related (more strongly in regions with complex topography) to enhanced cloud cover conditions (Walcek, 1994; Stensrud, 2009). As an attempt to aid the MOS model, bias correction was performed by separating the training functions into the following two subsets: above and below median surface relative humidity (RH). Current (before the forecasting day) relatively dry conditions (RH below RH50th percentile) relate well with clear-sky days, whereas during relatively wet conditions (RH above 50th percentile) such a relationship is not as clear. Overall, we found that this approach discriminates well during clear-sky days, avoiding unnecessary corrections by the MOS (e.g., when all moist regimes are considered together). Similar MOS approaches have been developed using step functions and multilinear regression approaches (Verzijlbergh et al., 2015) and show improvement in forecast accuracy.

**2.4.1.3. Moisture surges (Weather Function 2 or WxF2).** This weather function consists of adopting a process-oriented MOS system that includes a meaningful NAM regional-scale circulation pattern, which

in turn is related to an increase in cloud cover and rainfall (Seastrand et al., 2014; Mejia et al., 2016). The accuracy assessment using the WxF2 scenario focused only during July–Sept. Fig. 2 shows National Solar Radiation Database (NSRDB; Wilcox, 2007) data for Las Vegas during the 2004 NAM season. This highlights the tendency of “moisture surges”, such as the July 12–15 surge event (Rogers and Johnson, 2007; Mejia et al., 2010), to increase cloudiness. Note that moisture surges have a multi-day effect on incoming surface radiation (Fig. 2) and prompt a significant increase in the variability of late morning and afternoon irradiance (Fig. 3). We argue that the summertime diurnal variability exhibited in Fig. 3, which shows the strong predictability potential of solar irradiance, can further aid MOS strategies by compositing the outlined moisture surge, regional-scale circulation pattern.

We created a binary surge index following the Bordoni and Stevens (2006) approach, which captures the dominant synoptic variability

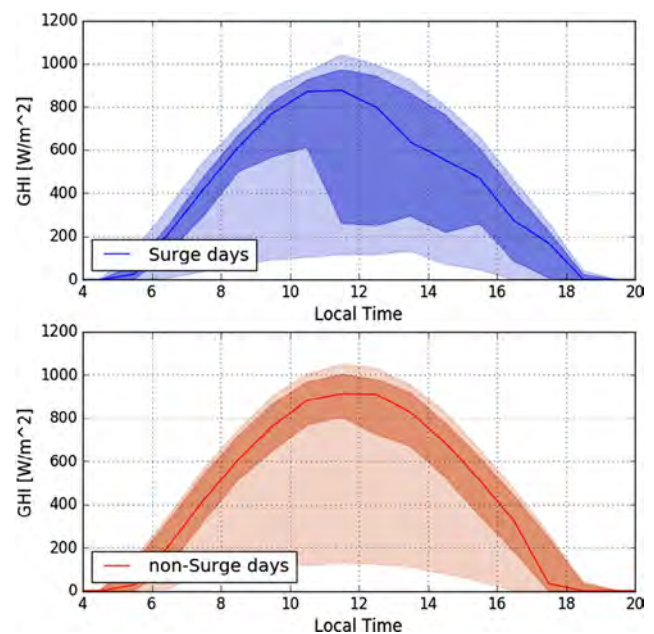


Fig. 3. Diurnal cycle distribution composites (extreme values, interquartile range, and median) of NREL/NSRDB modeled GHI averaged during the 2000–2005 NAM moisture surge/wet days (wet days; top panel) and non-moisture surge/dry days (following Mejia et al. (2016) moisture surge definition).

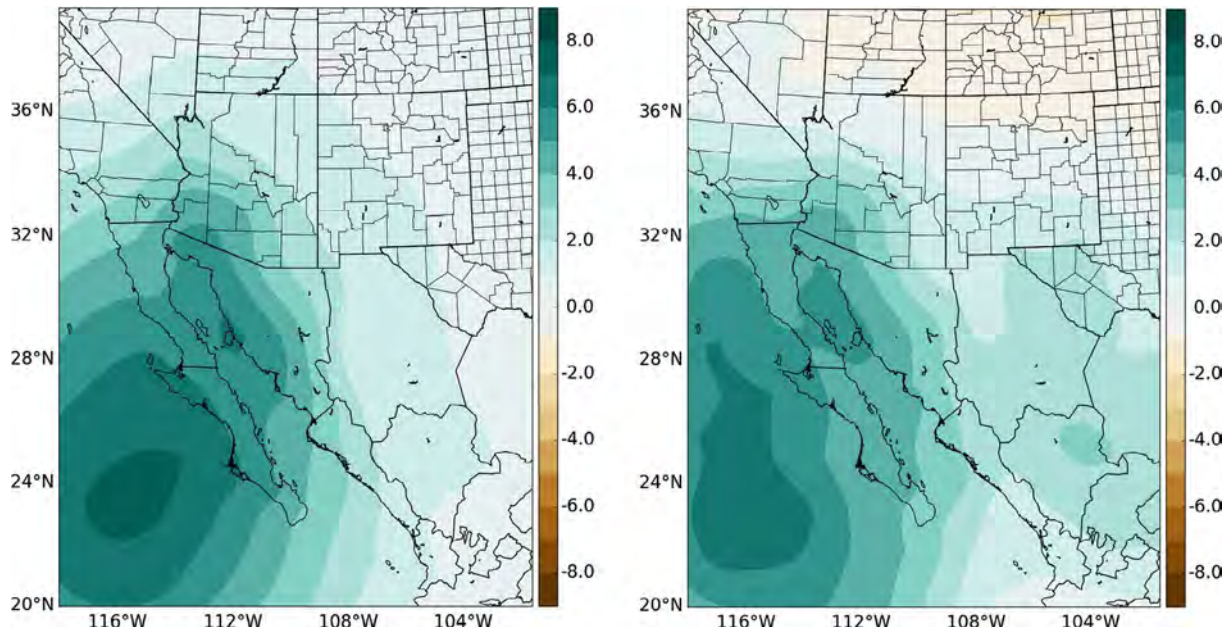


Fig. 4. Moisture composites estimated as surge days minus all days of total column water vapor [mm] for climatology (left; 1978–2016) and during the simulation period (right; 2015–2016) (see text for details in the compositing strategy).

mode, typically related to the southerly-southeasterly flow over the Gulf of California. We used GFS output (before the forecasting day) at 0.5 arcdeg, 10 m surface winds over the Gulf of California at 00 UTC. We performed a principal component analysis using archived data from July 2010 to the forecast day. The surge index enabled categorizing the leading principal component values exceeding one standard deviation as surge days; all other days were categorized as non-surge days. At the end of the assessment period, the leading principal component explained 47.2% of the variance, on average. Fig. 4 shows composited surge day differences (surge days minus all days) using the total column water vapor fields for the July to September monsoon season during a long-term period (2010–2016) and during the period (2015–2016) contrasting some differences in the surge impacts over the study region. Both composite periods, however, capture the relatively moist environments related to surge episodes.

### 2.4.2. MOS approaches

**2.4.2.1. Quantil-quantil mapping (Q-Q).** This MOS approach follows an empirical Quantil-quantil mapping method (hereafter, MOS Q-Q approach) adapted here for short-term NWP applications but originally developed for bias correction of regional climate variability and change products. The method is one of the most popular bias correction approaches because it is non-parametric, computationally efficient, and simple to implement (Mejia et al., 2012; Maraun, 2013; Hatchett et al., 2016). It consists of transforming the simulated cumulative distribution function (CDF) by adding the mean difference between the observed and model output at the corresponding quantiles. The MOS QQ assumes an equi-probability transformation between observations and model output empirical CDF. A significant limitation of this approach is that it does not perform well for extreme value and skew probability distribution functions (PDFs; e.g., hourly precipitation or wind gusts; Maraun, 2013).

**2.4.2.2. Linear regression.** A least square polynomial fit (of order 1 for linear fit; Wilks, 2011) is updated every forecasting cycle using either of the outlined training scenarios. The resultant polynomial coefficients help determine bias relative to the best fit, and are then applied to the future forecast and archived for retrospective simulated climatology estimates. An important underlying assumption in this approach is use of a Gaussian error distribution for assigning weights, which helps

avoid ill-conceived covariance matrices. In some cases, typically during strong intra-seasonal (~20 to 60 days) shifts, a quadratic fit has performed better than a linear polynomial (not shown). For simplicity, we have kept this MOS approach fixed with linear fit. Additional optimization opportunities may be available requiring additional research to adequately identify the flow regimes (weather functions) that introduce non-linear error structures in the model.

In summary, we implemented and examined four bias-correction scenarios using two MOS approaches (Q-Q and linear), including (i) without seasonally adjusting MOS; (ii) similar to (i) but discriminating with weather functions that include surface relative humidity (WxF1); (iii) seasonally adjusting MOS; (iv) similar to (iii) but discriminating with WxF1. During the monsoon season, only three scenarios were examined: (i) only considering the monsoon period and without weather functions; (ii) only monsoon and discriminating with WxF1; and (iii) only monsoon and discriminating with WxF2.

### 2.5. Error metrics

We implemented standard and basic solar power accuracy measurements to evaluate the model’s performance, allowing comparison between a sufficiently large number of pairs (N) of the model forecast (F) and the observed (O) hourly values (Zhang et al., 2013). We included the mean bias error (MBE); mean absolute error (MAE); root-mean-square error (RMSE); and the Pearson correlation coefficient (r), defined as follows:

$$MBE = \frac{1}{N} \sum_{i=1}^N (F_i - O_i)$$

$$rMBE = \frac{1}{N} \sum_{i=1}^N \left( \frac{F_i - O_i}{O_i} \right)$$

$$MAE = \frac{1}{N} \sum_{i=1}^N |F_i - O_i|$$

$$rMAE = \frac{1}{N} \sum_{i=1}^N \left| \frac{F_i - O_i}{O_i} \right|$$

$$RMSE = \sqrt{\frac{1}{N} \sum_{i=1}^N (F_i - O_i)^2}$$

$$rRMSE = \sqrt{\frac{1}{N} \sum_{i=1}^N \left( \frac{F_i - O_i}{O_i} \right)^2}$$

$$r = \frac{\sum_{i=1}^N (O_i - \bar{O})(F_i - \bar{F})}{\sqrt{\sum_{i=1}^N O_i - \bar{O}} \sqrt{\sum_{i=1}^N F_i - \bar{F}}}$$

The relative values of the MBE (rMBE), MAE (rMAE), and RMSE (rRMSE), which are estimated by normalization to the mean measured irradiance during a given period, also were considered to facilitate benchmarking against other studies and sites (Beyer et al., 2009; Mathiesen and Kleissl, 2011; Perez et al., 2013; Verzijlbergh et al., 2015). rMAE and rRMSE helped to assess the gain in performance of any specific approach and scenario and have been used in inter-comparison studies assessing forecast accuracy of different forecasting systems; and enabled us to compare performance in contrasting climates. Because the evaluation periods in different studies tend to be different, we used such benchmarking indices with caution. Alternatively, we compared the forecast against a simple reference model approach known as Persistence, which consists of using hourly observations from the current day to forecast the following day. Note that RMSE and rRMSE penalize large forecast errors, while MBE and MAE

treat errors uniformly. MAE- and MBE-related metrics are more associated with potential imbalances because of solar power generation systems (Zhang et al., 2013). An underlying assumption was that the error distribution was unbiased and followed a normal distribution.

### 3. Results

Table 2 shows detailed forecast accuracy evaluations contrasting error metrics, MOS approaches and scenarios, as well as model initialization times for the period August 1, 2015 to December 31, 2016. In general, the raw model output (WRF) and all the different implemented MOS scenarios and approaches outperformed the Persistence forecast, regardless of the error metric and season considered. The value added by the NWP approaches relative to the Persistence approach, for day-ahead solar forecasts or even longer forecast windows (2–5 days out), has been extensively discussed in the literature (Lauret et al., 2014; Perez et al., 2013). The Persistence forecast approach constitutes a simplistic model useful for benchmarking, but the NWP accuracy gain can be smaller in regions or seasons in which frequent and persistent multiday cloud structure can occur (i.e., wet and dry spells during the NAM), or characterized by a marked diurnal cycle of cloudiness.

In a comprehensive study to benchmark different NWP models and MOS GHI products, Perez et al. (2013) shows a set of forecast accuracy (normalized) metrics for the Desert Rock site (~100 km northwest of

Table 2

Day-ahead hourly GHI and Kt\* forecast accuracy during August 1, 2015 to December 31, 2016 (all analysis periods) for different error metrics, MOS approaches, and scenarios (see text for details). Analysis performed for WRF output at 2 km grid size and for initialization times starting at 00 and 12 UTC. Hatched cells indicate the best performing error metric among the different scenarios.

Parameter	Error Metric	(i) Not seasonally adjusted		(ii) Not seasonally adjusted and WxF1		(iii) Seasonal		(iv) Seasonal and WxF1	
		00 UTC	12 UTC	00 UTC	12 UTC	00 UTC	12 UTC	00 UTC	12 UTC
GHI	MBE [W/m <sup>2</sup> ]								
	Persistence	0.0	0.0	0.0	0.0	0.0	0.0	0.0	0.0
	WRF	72.8	69.7	72.8	69.7	72.8	69.7	72.8	69.7
	WRF+MOS Q-Q	0.56	0.53	0.41	0.39	0.1	0.20	0.013	0.086
	WRF+MOS Linear	0.46	0.49	-0.12	-0.01	0.64	0.37	0.167	-0.119
Kt*	MBE								
	Persistence	0.0	0.0	0.0	0.0	0.0	0.0	0.0	0.0
	WRF	0.161	0.158	0.161	0.158	0.161	0.158	0.161	0.158
	WRF+MOS Q-Q	-0.034	-0.031	-0.033	-0.030	-0.033	-0.029	-0.030	-0.027
	WRF+MOS Linear	-0.004	0.010	0.013	0.031	-0.002	0.003	0.002	0.006
GHI	rMAE [%]								
	Persistence	20.9	20.6	20.9	20.6	20.9	20.6	20.9	20.6
	WRF	18.5	18.5	18.5	18.5	18.5	18.5	18.5	18.5
	WRF+MOS Q-Q	18.0	17.8	17.6	17.3	17.9	17.7	17.13	16.84
	WRF+MOS Linear	18.4	18.3	17.6	17.5	18.2	18.0	17.12	16.91
Kt*	rMAE [%]								
	Persistence	22.9	22.7	22.9	22.7	22.9	22.7	22.9	22.7
	WRF	21.1	21.3	21.1	21.3	21.1	21.3	21.1	21.3
	WRF+MOS Q-Q	21.6	21.2	20.9	20.6	21.1	20.7	20.11	19.66
	WRF+MOS Linear	20.7	20.2	20.2	20.8	20.3	20.2	19.21	19.33
GHI	rRMSE [%]								
	Persistence	36.1	36.0	36.1	36.0	36.1	36.0	36.1	36.0
	WRF	32.0	32.2	32.0	32.2	32.0	32.2	32.0	32.2
	WRF+MOS Q-Q	27.9	28.3	27.5	27.8	28.0	28.4	27.44	27.76
	WRF+MOS Linear	27.1	27.5	26.3	26.6	26.9	27.4	25.92	26.23
Kt*	rRMSE [%]								
	Persistence	36.4	36.2	36.4	36.2	36.4	36.2	36.4	36.2
	WRF	33.4	33.7	33.4	33.7	33.4	33.7	33.4	33.7
	WRF+MOS Q-Q	28.9	28.9	28.5	28.5	28.8	28.8	28.31	28.20
	WRF+MOS Linear	28.2	28.4	28.0	29.6	28.0	28.5	27.08	27.75
GHI	r								
	Persistence	0.70	0.70	0.70	0.70	0.70	0.70	0.70	0.70
	WRF	0.81	0.80	0.81	0.80	0.81	0.80	0.81	0.80
	WRF+MOS Q-Q	0.81	0.81	0.82	0.81	0.81	0.81	0.8	0.81
	WRF+MOS Linear	0.81	0.80	0.82	0.82	0.81	0.81	0.8	0.82
Kt*	r								
	Persistence	0.27	0.28	0.27	0.28	0.27	0.28	0.27	0.28
	WRF	0.39	0.39	0.39	0.39	0.39	0.39	0.39	0.39
	WRF+MOS Q-Q	0.39	0.41	0.42	0.43	0.42	0.43	0.45	0.46
	WRF+MOS Linear	0.40	0.39	0.43	0.39	0.41	0.41	0.46	0.46

Las Vegas) that help contrast our results for the NREL-UNLV site. Perez et al. (2013) used year-long GHI forecast products (May 1, 2009 to April 30, 2010) and estimated that the error associated with Persistence at 00 UTC was 19% for rMAE and 29% for rRMSE. In contrast, our NREL-UNLV site is 20.9% for rMAE and 36.1% for rRMSE. Although both sites are located in regions exposed to arid climate environments and surrounded by complex terrain, differences in the Persistence approach could also be attributed to factors that include local cloud forcing and interannual climate variations. Larger Persistence error metrics suggested higher cloudiness variability at the NREL-UNLV site than around the Desert Rock area.

Fig. 6 and Table 2 show that both MOS Q-Q and MOS linear approaches effectively removed the GHI MBE, while also improving overall error metrics. MOS GHI accuracy improved 2.8–3.6% for rMAE and 4.7–5.8% for rRMSE. Our results also showed that the MOS linear approach outperformed MOS Q-Q by small margins (~1%) when considering rMAE and rRMSE. The MOS approaches are efficient techniques for removing bias and improving the overall accuracy when model products show systematic errors (Verzijlbergh et al., 2015; Perez et al., 2013). For example, Perez et al. (2013) showed MOS GHI accuracy gains relative to a set of NWP models implemented at the Desert Rock site ranging from 2% to 8% for rMAE and 2% to 9% for rRMSE.

The results presented here and other studies highlight the

fundamental role of MOS tools in improving the accuracy of NWP systems for solar irradiance forecasting. In agreement with Voyant et al. (2015), our results also show that the effectiveness of any MOS tool can vary more notably across different locations than the differences among the MOS approaches themselves at any one site. Additionally, the magnitude of the improvements appears to be slightly sensitive (~2%) to the training scenarios (Section 2.4.1), with a consistent tendency to improve accuracy in all error metrics when training the MOS using the seasonally adjusted and WxF1 scenarios, as shown by the hatched cells in Table 2. Similar gains were shown in Verzijlbergh et al. (2015) when using alternative weather parameters (RMSE = 40%) relative to standard methods (RMSE = 43%) that use the GHI observations to correct the bias in forecasted GHI.

Our results showed a small difference in the model’s performance when considering the initialization times (00 UTC and 12 UTC). The 00 UTC outperformed 12 UTC model output for all accuracy metrics by 0.1–0.5%, except for GHI MBE, that tended to be larger for initializations at 00 UTC by up to 3 W/m<sup>2</sup>. Consistent with Perez et al. (2013), however, there were no measurable advantage apparent between the initialization times after MOS was applied.

Our focus was to show the overall impact of training MOS GHI and Kt\* forecasts by compositing with meaningful regional synoptic patterns (WxF2) that are related to increased cloud variability in the Las

**Table 3**  
Day-ahead hourly GHI and Kt\* forecast accuracy during the August 1, 2015 to September 30, 2016 and July 1, 2016 to September 30, 2016 (only available North American Monsoon season periods) for different error metrics, MOS approaches, and scenarios (see text for details). Analysis performed for WRF output at 2 km grid size and for initialization times starting at 00 and 12 UTC. Hatched cells indicate the best performing error metric among the scenarios.

Parameter	Error Metric	Monsoon		Monsoon and WxF1		Monsoon and WxF2	
		00 UTC	12 UTC	00 UTC	12 UTC	00 UTC	12 UTC
GHI	MBE [W/m <sup>2</sup> ]	0.00	0.00	0.00	0.00	0.00	0.00
	Persistence	0.00	0.00	0.00	0.00	0.00	0.00
	WRF	66.43	65.95	66.43	65.95	63.60	67.03
	WRF+MOS Q-Q	-1.48	0.34	2.13	2.72	-0.50	0.85
	WRF+MOS Linear	-11.02	-9.04	-4.56	-4.67	-2.52	-0.50
Kt*	MBE	0.00	0.00	0.00	0.00	0.00	0.00
	Persistence	0.00	0.00	0.00	0.00	0.00	0.00
	WRF	0.14	0.14	0.14	0.14	0.16	0.16
	WRF+MOS Q-Q	-0.02	-0.02	-0.03	-0.04	-0.02	-0.01
	WRF+MOS Linear	-0.03	-0.02	-0.01	-0.01	0.00	0.00
GHI	rMAE [%]						
	Persistence	15.01	15.08	15.01	15.08	15.06	15.30
	WRF	14.02	14.42	14.02	14.42	14.26	14.94
	WRF+MOS Q-Q	13.16	13.42	12.86	13.20	12.66	13.09
	WRF+MOS Linear	14.52	14.82	13.68	14.16	12.98	13.45
Kt*	rMAE [%]						
	Persistence	17.75	17.94	17.75	17.94	17.70	18.00
	WRF	17.65	18.47	17.65	18.47	20.71	21.66
	WRF+MOS Q-Q	19.57	19.44	19.57	20.52	19.31	19.83
	WRF+MOS Linear	18.40	18.80	17.43	18.26	16.85	17.24
GHI	rRMSE [%]						
	Persistence	27.93	28.16	27.93	28.16	28.05	28.56
	WRF	24.62	25.56	24.62	25.56	24.84	26.29
	WRF+MOS Q-Q	21.88	22.73	21.78	22.61	21.85	22.76
	WRF+MOS Linear	21.27	22.16	21.34	22.17	21.00	21.68
Kt*	rRMSE [%]						
	Persistence	30.48	30.93	30.48	30.93	30.58	31.03
	WRF	28.56	29.75	28.56	29.75	31.33	32.97
	WRF+MOS Q-Q	29.95	29.86	30.37	31.79	30.69	31.57
	WRF+MOS Linear	24.17	24.92	24.17	25.03	23.61	24.46
GHI	r						
	Persistence	0.44	0.44	0.44	0.44	0.44	0.44
	WRF	0.57	0.56	0.57	0.56	0.58	0.55
	WRF+MOS Q-Q	0.58	0.56	0.58	0.57	0.60	0.60
	WRF+MOS Linear	0.57	0.56	0.57	0.56	0.61	0.61
Kt*	r						
	Persistence	0.24	0.25	0.24	0.25	0.24	0.25
	WRF	0.32	0.33	0.32	0.33	0.32	0.33
	WRF+MOS Q-Q	0.38	0.39	0.36	0.38	0.39	0.40
	WRF+MOS Linear	0.32	0.33	0.31	0.33	0.42	0.44

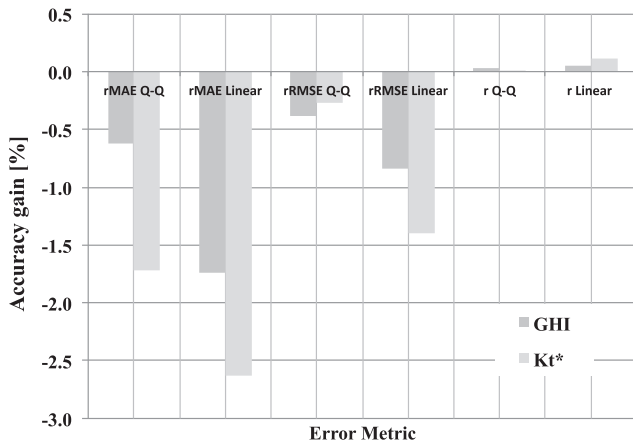


Fig. 5. NAM GHI and Kt\* forecast metric difference (seasonally adjusted discriminating with WxF2 minus seasonally adjusted only). Only August to September 2005 and July to September 2016 are considered.

Vegas area. Table 3 shows accuracy error statistics during the NAM periods for three different training scenarios. In general, improvements in the error patterns described earlier (Table 2) tend to hold during the NAM season with few exceptions. A striking result is that NAM GHI rMAE and rRMSE reduced by 1 m–2% from the seasonally adjusted scenario to the seasonally adjusted discriminating with WxF2 scenario. Additionally, discriminating with WxF2 increased GHI r from 0.5 to 0.57.

Fig. 5 summarizes the forecast accuracy yielded by the proposed approaches during the NAM season. Kt\* accuracy gains were better than those using the GHI across the different error metrics. The solar forecast accuracy using WxF2 improved all error metrics with MOS linear approach outperforming the MOS Q-Q approach. Despite k<sub>t</sub>\* being defined as a non-stationary parameter, further benefits were gained when the seasonally adjusted scenario was applied. The WxF1

and WxF2 scenarios also enhanced forecast accuracy using the k<sub>t</sub>\* parameter.

Fig. 6 shows that the GHI high-bias structure appeared to be linear and proportional to the GHI intensity with apparent lower performance during observed cloudy days. However, the clear-sky index tends to be bimodal (Reno et al., 2012), with relatively high frequency of very cloudy hours and clear sky values. With lower frequency of intermediate values, the clear-sky index transformation appears to be more effective in accuracy gains.

Figs. 6 and 7 show the error statistics for the mean diurnal cycle using the seasonally adjusted WxF1 scenario. Not surprisingly, rMBE results show that Persistence is unbiased throughout the day, and again, the raw model and MOS approach outperformed Persistence in all other evaluated metrics, except for late afternoon when Persistence tended to improve. This likely was because of the marked diurnal cycle (Fig. 3). The model showed an asymmetrical error structure with the best performance around 10–12 LST, and the worst performance during afternoon hours. This could be explained by the nature of afternoon cumulus and cumulonimbus clouds. Lower performance during the afternoon can be related to afternoon surface heating that supports lower troposphere mixing and atmospheric boundary layer convective clouds (Kim et al., 2016). These features are more pronounced during the warm season, including regions with arid and semiarid climates (Alessandrini et al., 2015). Fortunately, the model performed better during high solar elevation angles, but the poorer performance during low solar elevation angles limited the ability to schedule solar power when an afternoon power ramp is expected (Shedd et al., 2012).

Another striking result in Figs. 6 and 7 is that the MOS linear approach outperformed the MOS Q-Q approach for both GHI and k<sub>t</sub>\*. Figs. 6 and 7 showed a near zero rMBE for MOS Q-Q when averaged throughout the study period. To some extent, this was true for all scenarios examined with mean residual differences well below 1 W/m<sup>2</sup>. Mean diurnal cycle showed that such error was the product of bias compensation during the day, however, with negative (positive) GHI (K<sub>t</sub>\*) rMBE during low solar elevation angles and positive (negative)

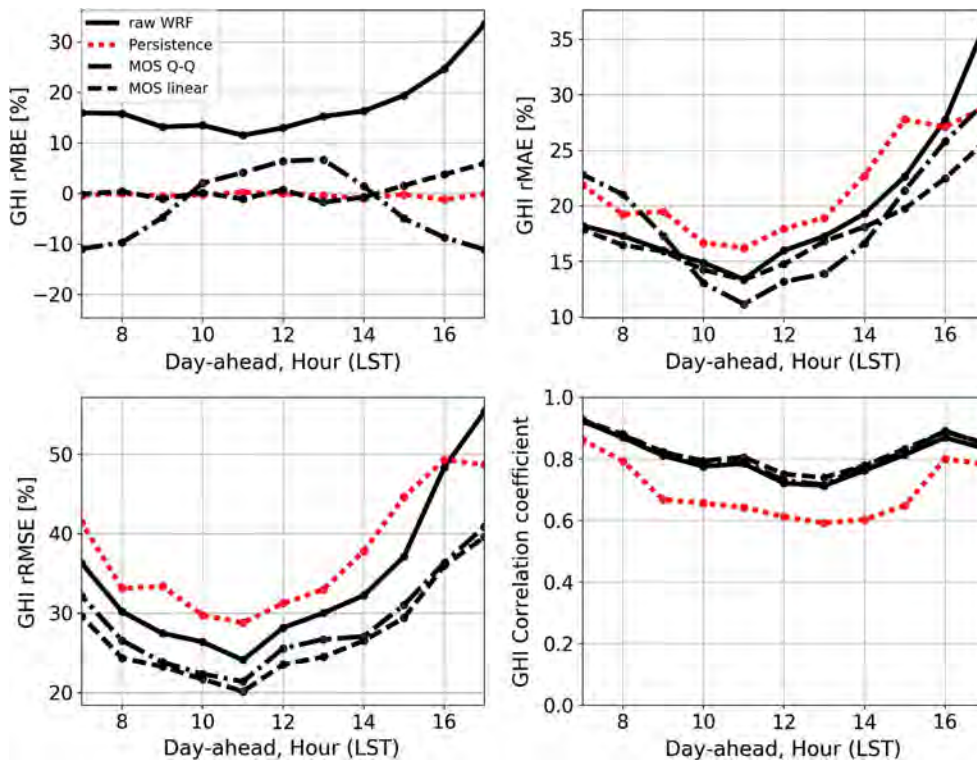


Fig. 6. Day-ahead GHI rMBE (upper-left panel), rMAE (upper-right panel), rRMSE (lower-left) and r (lower-right) for Persistence, raw WRF model, and seasonally adjusted MOS Q-Q and linear approaches. Forecast valid for NREL-UNLV at 00 UTC.

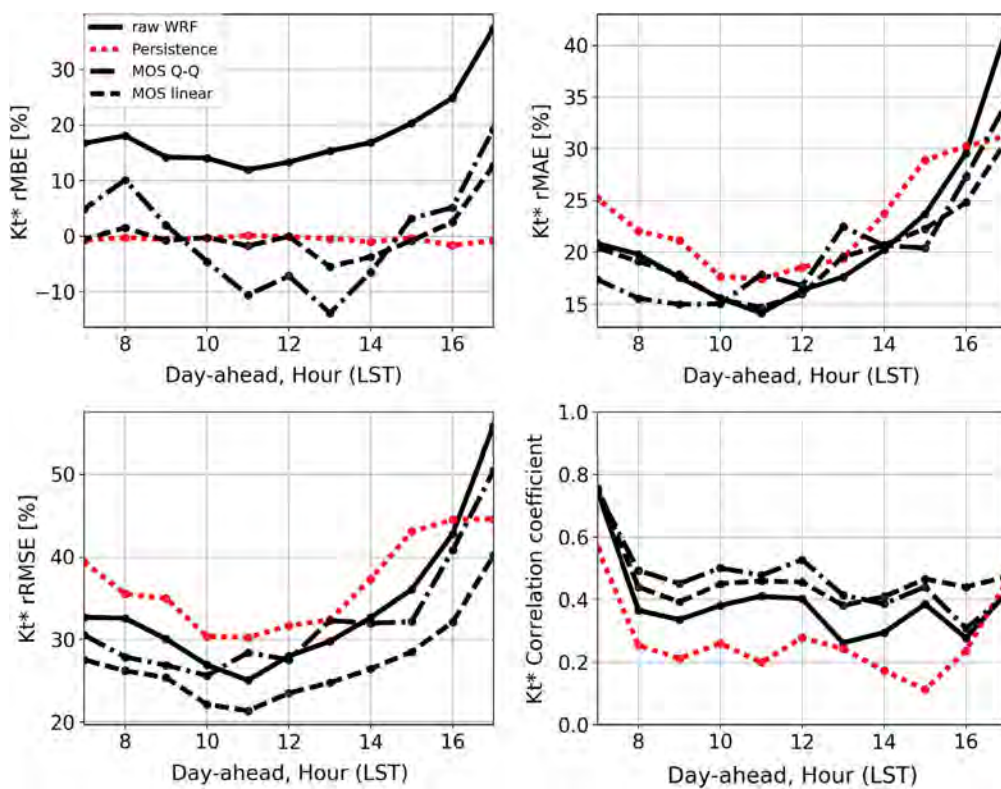


Fig. 7. Same as in Fig. 6 but for the  $K_t^*$  parameter.

rMBE during high elevation angles. The MOS linear approach was unbiased during most of the day, except for a small, positive late afternoon GHI and  $K_t^*$  rMBE.

Fig. 8 shows error rMBE per month and hour of day, highlighting that GHI and  $K_t^*$  high biases are positive and systematic throughout the year and during the day (with an all time mean GHI and  $K_t^*$  rMBE of +18% and 17.6%).

Both the GHI and  $K_t^*$  high biases showed a seasonal dependence with larger magnitude during the spring and summer seasons, likely related to increased storminess and moisture transport associated with the passage of troughs and closed lows in the spring and early summer

(Oakley and Redmond, 2014) and the NAM in July–September (Mejia et al., 2016). These biases exposed structural issues in the WRF model output, that may be avoided by improving its integration configuration and using other model physics. One note is that other studies have found that GFS, which is used to drive the WRF model, also tends to have a GHI positive bias during clear sky conditions, when averaged over the U.S. CONUS (Mathiesen and Kleissl, 2011). However, GFS may have significantly changed as several structural technological improvements have been made since then, including the resolution and data assimilation system. Examining the reasons for such model deficiencies, either in the GFS or regional WRF model, is a challenging task and is outside the scope of this study. Model systematic error, however, allows for MOS to be used to produce a bias-corrected forecast. Fig. 9 also show that MOS linear provides a more uniform bias correction with less monthly and diurnal dependency.

Figs. 10 and 11 show the overall accuracy gain in GHI and  $K_t^*$ , respectively, estimated as the difference between MOS minus the raw WRF error, using MOS Q-Q and linear with the seasonally adjusted WxFl scenario. Of note is that the MOS linear approach tended to perform better, as measured by rMAE and rRMSE, and more uniformly in time than the Q-Q approach. Furthermore, GHI accuracy showed losses that tended to occur at low sun elevation angles during the day, whereas  $K_t^*$  showed accuracy losses that tended to occur during high sun elevation angles. The seasonal and diurnal distribution of accuracy metrics confirmed that the bias corrections on the  $K_t^*$  parameter tended to respond better than the GHI. Additionally, MOS linear in combination with the seasonally adjusted scenario tended to provide better forecast irradiance results than the Q-Q approach.

#### 4. Discussion and conclusion

We developed a procedure that can be used to improve the accuracy of day-ahead NWP-based GHI and  $K_t^*$  forecasts for NREL-UNLV, an observation site located in Las Vegas, Nevada by performing a detailed forecast error assessment using 17 months of real-time GHI forecast

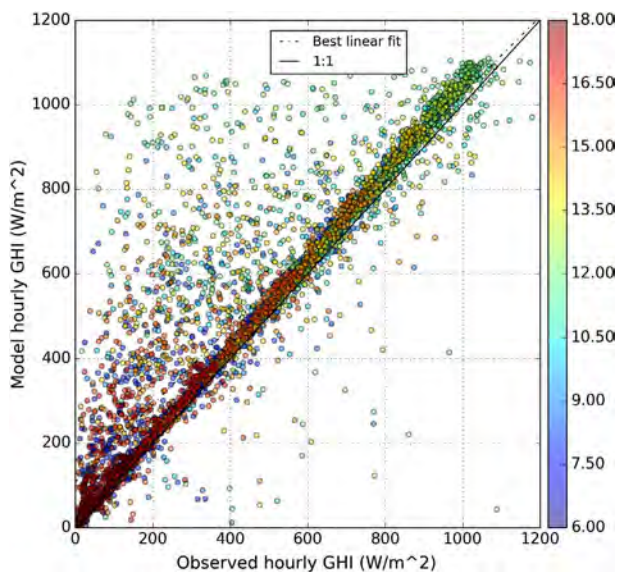


Fig. 8. Hourly day-ahead GHI and raw WRF model pairs at 00 UTC color coded by hour of the day.

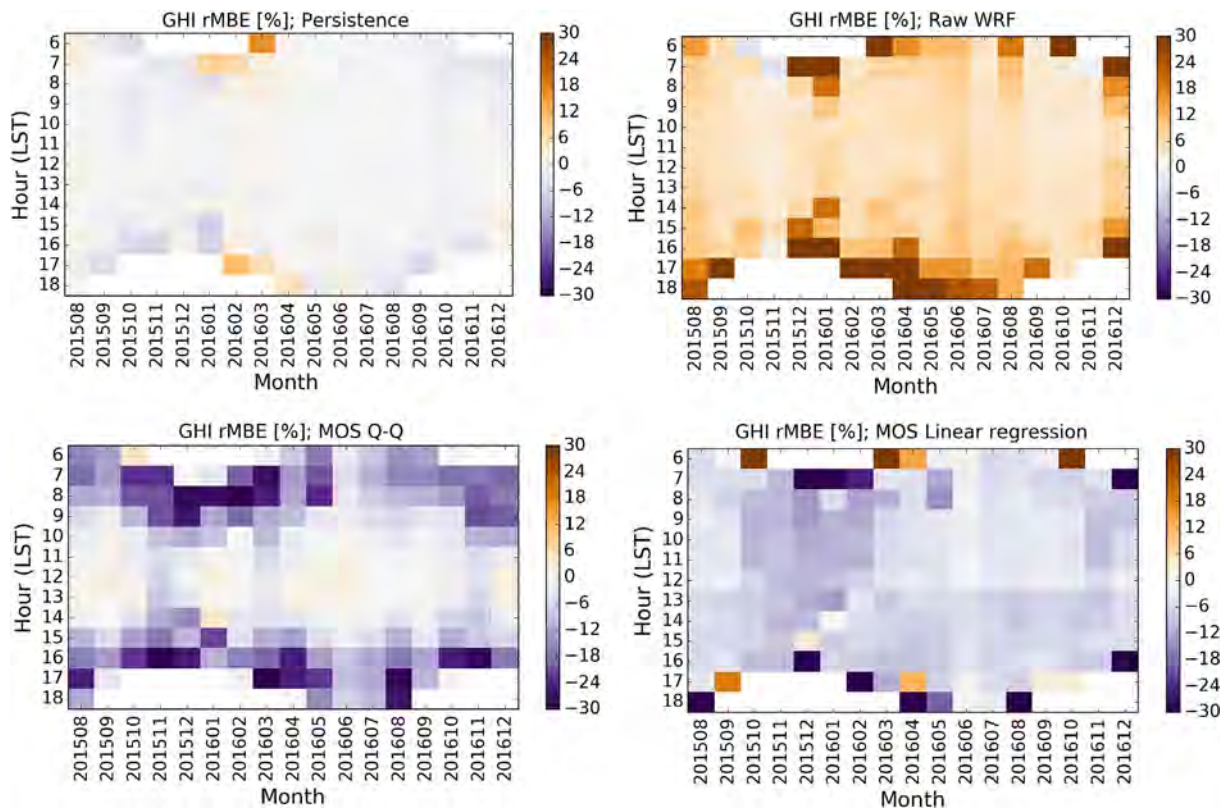


Fig. 9. Day-ahead hourly GHI rMBE per month [YYYYMM] and per hour [LST] for Persistence (upper-left panel), raw WRF model (upper-right panel), and MOS Q-Q (lower-left panel) and linear approaches (upper-right panel) using seasonally adjusted WxFl scenario. Forecast valid for NREL-UNLV at 00 UTC.

products. The improvements were performed by conditioning the GHI forecasts to post-processing procedures consisting of MOS approaches and to training scenarios that are seasonally adaptive and incorporate moist states and regional weather circulation patterns.

The MOS approaches and training scenario strategies proved to be effective tools to correct systematic biases in the model, but also discriminated the error structure and timing of the convective processes using weather functions that relate the regional weather patterns that drive cloudiness variability in the area of interest. These post-processing procedures helped us objectively interpret and improve NWP-based GHI and  $Kt^*$  forecasts for the NREL-UNLV site. Understanding the NWP-based error structure can potentially improve solar forecasts from NWP. The procedures outlined here can be useful for other locations in the southwestern U.S., where GHI forecast errors are affected by the NAM. A limitation in the described approach is that additional data are required to estimate the regional weather circulation patterns related to NAM moisture surges. Additionally, model versions may change more frequently than the record length needed for robust weather functions (the adaptive approach of the seasonally adjusted scenario can mitigate part of this issue). The moisture transient processes related to the NAM, processes that are observable and predictable –at least for the day-ahead forecasting window–prove to be fundamental in unveiling the value of solar forecasts in the region.

In general, we stress that development of higher-resolution NWP GHI and  $Kt^*$  products is justifiable as the WRF model includes improved bottom boundary conditions (land use, vegetation coverage, topography, land/water mask) relative to its global initial and boundary condition driver; and more complex processes with more sophisticated schemes and realistic detail (e.g., explicit convection/cloud resolving scales). Of note is that both the raw model output and MOS forecasts add value when compared to Persistence. Using day-ahead NWP-based GHI forecasts involved intricate model error characteristics, however, with measurable uncertainties that depend on the season and time of day.

MOS implementation was fundamental to removing model systematic biases and the trend in accuracy gain appears to be sensitive to MOS approaches and scenarios. The magnitude of the trends was marginal, and more work is required to incorporate more meaningful and intelligent weather functions to better discern the error structure in cloudiness. Alternatively, GHI and  $Kt^*$  forecasts appear to be independent of the forecast initialization time. The relatively low sensitivity of training scenarios in the accuracy (< 2–3%) of the model and the systematic errors suggests some stationarity in the variability of the data. However, model tends to perform better in the morning and around noon than during the afternoon). Results for both the GHI and  $Kt^*$  support that MOS linear outperforms the MOS Q-Q approach, with larger accuracy gains shown by the  $Kt^*$  parameter. These results suggest that  $Kt^*$  could be used to help improve GHI forecasts, as supported by [Reno et al. \(2012\)](#).

Systematic high GHI biases suggest that testing other driving global NWP systems or other regional NWP model configurations and physics are warranted. Further work is necessary for developing weather functions relating the cloudiness from other synoptic transients and local conditions during different seasons, as shown by the relatively low NWP-based GHI accuracy during spring. The sensitivity around MOS approaches and training strategies, although marginal in some cases, can help create dispersive ensemble model output statistic solutions (EMOS; [Sperati et al., 2016](#)). Benefits of a MOS-based ensemble approach are clear because of their high efficiency compared to global and regional NWP ensembles. Alternatively, we plan to apply the described concepts to other sites and regions and argue that the training scenarios based on seasonal adaptation of the MOS are transferable to any region (where annual variability in cloudiness is large, and the flow regimes can change the cloud frequency, type, and formation processes – including other local variability drivers, such as smoke, mineral aerosols, etc.). Next, we plan to complete an assessment of the benefits of NWP-based GHI forecasts on power output and ramps.

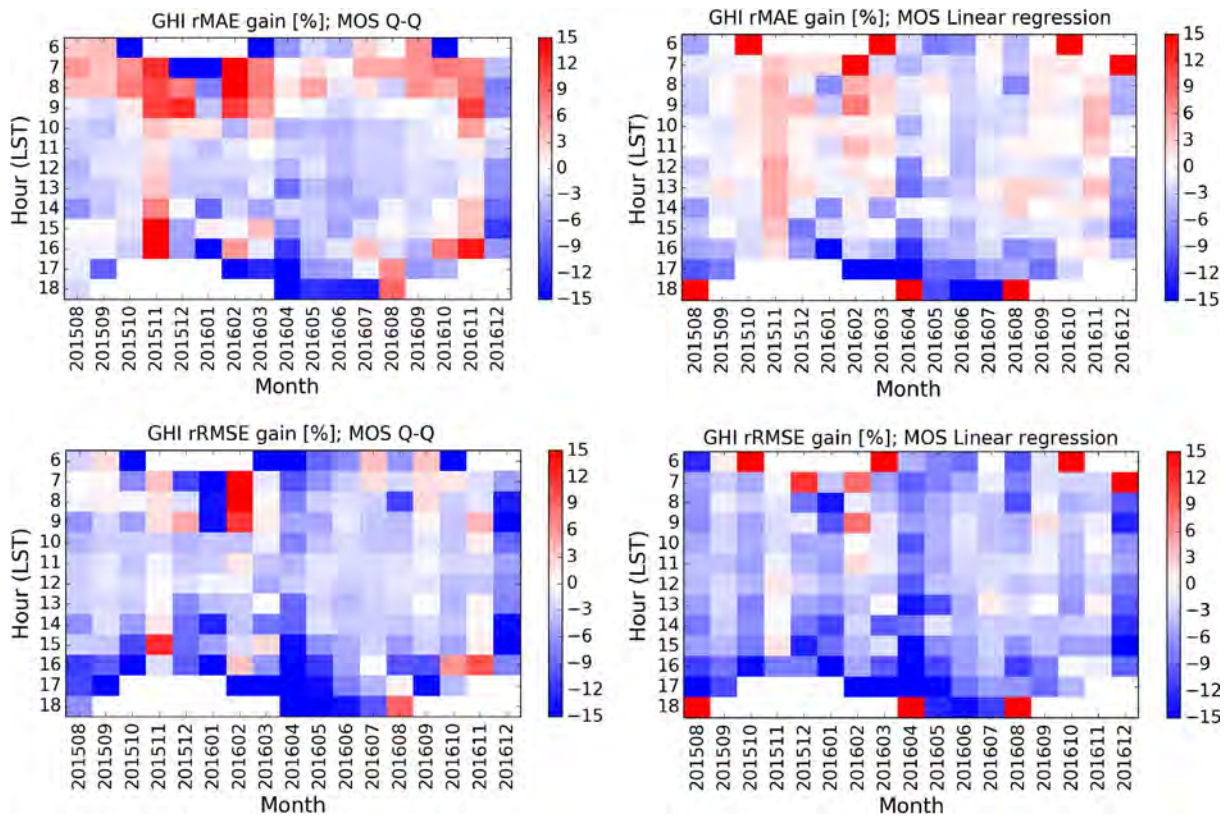


Fig. 10. Day-ahead hourly GHI rMAE (top panels) and rRMSE (bottom panels) differences for MOS Q-Q raw (left panels) or MOS linear (right panels) minus raw WRF model per month [YYYYMM] and per hour [LST] using the seasonally adjusted WxFl scenario. Forecast valid for NREL-UNLV at 00 UTC. Negative (positive) values indicate a net gain (loss) in the accuracy metric by implementing the MOS approach and scenario relative to the raw WRF model.

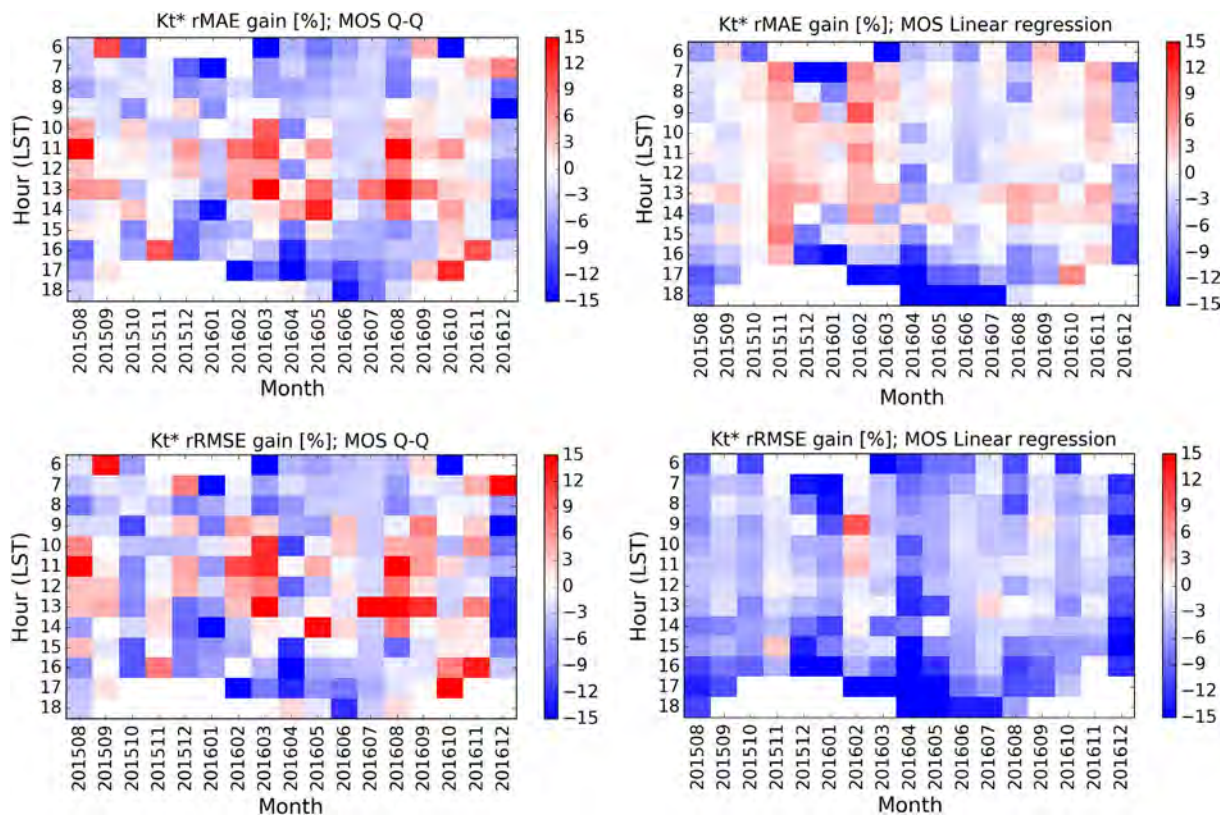


Fig. 11. Same as in Fig. 9 but for Kt\*.

## Acknowledgments

This material is based upon work sponsored by the Nevada Governor's Office of Economic Development, and by the National Science Foundation-United States under Grant No. IIA-1301726. Surface observations for validation were downloaded from the National Renewable Energy Laboratory-University of Nevada, Las Vegas data repository.

## References

- Adams, D.K., Comrie, A.C., 1997. The North American monsoon. *Bull. Am. Meteorol. Soc.* 78, 2197–2213.
- Akaraslan, E., Hocaoglu, F.O., 2016. A novel adaptive approach for hourly solar radiation forecasting. *Renew. Energy* 87, 628–633.
- Alessandrini, Alessandrini S., Delle Monache, L., Sperati, S., Cervone, G., 2015. An analog ensemble for short-term probabilistic solar power forecast. *Appl. Energy* 157, 95–110. <http://dx.doi.org/10.1016/j.apenergy.2015.08.011>. ISSN 0306-2619.
- Andreas, A., Stoffel, T., 2006. University of Nevada (UNLV): Las Vegas, Nevada (Data); NREL Report No. DA-5500-56509.
- Badosa, J., Haeffelin, Martial, Kalecinski, Natacha, Bonnardot, François, Jumaux, Guillaume, 2015. Reliability of day-ahead solar irradiance forecasts on Reunion Island depending on synoptic wind and humidity conditions. *Solar Energy. Sol. Energy* 115 (May), 306–321. <http://dx.doi.org/10.1016/j.solener.2015.02.039>. ISSN 0038-092X.
- Benjamin, S.G., et al., 2004. An hourly assimilation–forecast cycle: the RUC. *Mon. Weather Rev.* 132, 495–518.
- Beyer, Georg, Hans, Polo Martinez, J., Suri, Marcel, Torres, Jose Luis, Lorenz, Elke, Müller, Stefan C., Hoyer-Klick, Carsten, Ineichen, Pierre, 2009. Report on Benchmarking of Radiation Products. Management and Exploitation of Solar Resource Knowledge Report under contract 038665.
- Bordoni, S., Stevens, B., 2006. Principal component analysis of the summertime winds over the Gulf of California: a gulf surge index. *Mon. Weather Rev.* 134, 3395–3414.
- Chow, J.C., John, G., Watson, Mark C., Green, Douglas H., Lowenthal, David W., DuBois, Steven D., Kohl, Richard T., Egami, John Gillies., Fred Rogers, C., Frazier, Clifton A., Cates, William., 1999. Middle- and neighborhood-scale variations of PM10 source contributions in Las Vegas, Nevada. *J. Air Waste Manage. Assoc.* 49 (6), 641–654. <http://dx.doi.org/10.1080/10473289.1999.10463837>.
- Cui, B., Toth, Z., Zhu, Y., Hou, D., 2012. Bias correction for global ensemble forecast. *Weather Forecast.* 27 (2), 396–410.
- Diagne, M., David, M., Boland, J., Schmutz, N., Lauret, P., 2014. Post-processing of solar irradiance forecasts from WRF model at Reunion Island. *Sol. Energy* 105, 99–108.
- Dorman, C.E., Mejia, J.F., Koracin, D., 2013. Impact of US west coastline inhomogeneity and synoptic forcing on winds, wind stress, and wind stress curl during upwelling season. *J. Geophys. Res. Oceans* 118 (9), 4036–4051.
- Dudhia, J., 1989. Numerical study of convection observed during the Winter Monsoon Experiment using a mesoscale two-dimensional model. *J. Atmos. Sci.* 46, 3077–3107.
- Fernández-González, S., Valero, F., Sánchez, J.L., Gascón, E., López, L., García-Ortega, E., Merino, A., 2015. Numerical simulations of snowfall events: sensitivity analysis of physical parameterizations. *J. Geophys. Res. Atmos.* 120, 10130–10148. <http://dx.doi.org/10.1002/2015JD023793>.
- Glahn, H.R., Lowry, D.A., 1972. The use of Model Output Statistics (MOS) in objective weather forecasting. *J. Appl. Meteor.* 11, 1203–1211. [http://dx.doi.org/10.1175/1520-0450\(1972\)011<1203:TUOMOS>2.0.CO;2](http://dx.doi.org/10.1175/1520-0450(1972)011<1203:TUOMOS>2.0.CO;2).
- Hatchett, Benjamin J., Koracin, Darko., Mejia, John F., Boyle, Douglas P., 2016. Assimilating urban heat island effects into climate projections. *J. Arid Environ.* 128, 59–64. <http://dx.doi.org/10.1016/j.jaridenv.2016.01.007>. ISSN 0140-1963.
- Higgins, R.W., Shi, W., 2001. Intercomparison of the principal modes of interannual and intraseasonal variability of the North American monsoon system. *J. Clim.* 14, 403–417.
- Holmgren, W.F., Groenendyk, D.G., 2016. An Open Source Solar Power Forecasting Tool Using PVLIB-Python. In: 43rd Photovoltaic Specialists Conference. [http://pvlib-python.readthedocs.io/en/latest/package\\_overview.html](http://pvlib-python.readthedocs.io/en/latest/package_overview.html). <http://dx.doi.org/10.5439/1052548>; <https://www.nrel.gov/midc/unlv/>.
- Ineichen, P., Perez, R., 2002. A new airmass independent formulation for the Linke turbidity coefficient. *Sol. Energy* 73, 151–157.
- Jacks, E., Bower, J.B., Dagostaro, V.J., Dallavalle, J.P., Erickson, M.C., Su, J.C., 1990. New NGM-based MOS guidance for maximum/minimum temperature, probability of precipitation, cloud amount, and surface wind. *Weather Forecast.* 5 (1), 128–138.
- Janjic, Zavisla I., 1994. The Step-Mountain Eta Coordinate Model: further developments of the convection, viscous sublayer, and turbulence closure schemes. *Mon. Weather Rev.* 122, 927–945.
- Jimenez, Pedro A., Hacker, Joshua P., Dudhia, Jimmy., Haupt, Sue Ellen., Ruiz-Arias, Jose A., Gueymard, Chris A., Thompson, Gregory., Eidhammer, Trude., Deng, Aijun., 2016. WRF-Solar: description and clear-sky assessment of an augmented NWP model for solar power prediction. *Bull. Am. Meteorol. Soc.* 97 (7), 1249–1264.
- Johnson, R.H., Ciesielski, P.E., McNoldy, B.D., Rogers, P.J., Taft, R.K., 2007. Multiscale variability of the flow during the North American Monsoon Experiment. *J. Clim.* 20 (9), 1628–1648.
- Kim, C.K., Leuthold, M., Holmgren, W.F., Cronin, A.D., Betterton, E.A., 2016. Toward improved solar irradiance forecasts: a simulation of deep planetary boundary layer with scattered clouds using the weather research and forecasting model. *Pure Appl. Geophys.* 173 (2), 637–655.
- Kim, C.K., Clarkson, M., 2016. Toward improved solar irradiance forecasts: introduction of post-processing to correct the direct normal irradiance from the weather research and forecasting model. *Pure Appl. Geophys.* 173 (5), 1751–1763. <http://dx.doi.org/10.1007/s00024-015-1203-x>.
- Lauret, P., Diagne, Maimouna, David, Mathieu, 2014. A neural network post-processing approach to improving NWP solar radiation forecasts. *Energy Procedia* 57, 1044–1052. <http://dx.doi.org/10.1016/j.egypro.2014.10.089>. ISSN 1876-6102.
- Leung, L.R., Qian, Y., Bian, X., 2003. Hydroclimate of the western United States based on observations and regional climate simulation of 1981–2000. Part I: seasonal statistics. *J. Clim.* 16 (12), 1892–1911.
- Liang, Xin-Zhong, Min, Xu, Yuan, Xing, Ling, Tiejun, Choi, Hyun I., Zhang, Feng, Chen, Ligang, Liu, Shuyan, Shenjian, Su, Qiao, Fengxue, He, Yuxiang, Wang, Julian X.L., Kunkel, Kenneth E., Gao, Wei, Joseph, Everette, Morris, Vernon, Tsann-Wang, Yu, Dudhia, Jimmy, Michalakes, John, 2012. Regional climate-weather research and forecasting model. *Bull. Am. Meteorol. Soc.* 93, 1363–1387. <http://dx.doi.org/10.1175/BAMS-D-11-00180.1>.
- Liou, K.N., Gu, Y., Leung, L.R., Lee, W.L., Fovell, R.G., 2013. A WRF simulation of the impact of 3-D radiative transfer on surface hydrology over the Rocky Mountains and Sierra Nevada. *Atmos. Chem. Phys.* 13 (23), 11709–11721.
- Lorenz, E., Hurka, J., Heinemann, D., Beyer, H.G., 2009. Irradiance forecasting for the power prediction of grid-connected photovoltaic systems. *IEEE J. Sel. Top. Appl. Earth Obs. Remote Sens.* 2 (1), 2–10.
- Maraun, D., 2013. Bias correction, quantile mapping, and downscaling: revisiting the inflation issue. *J. Clim.* 26 (6), 2137–2143.
- Mathiesen, Patrick, Kleissl, Jan., 2011. Evaluation of numerical weather prediction for intra-day solar forecasting in the continental United States. *Sol. Energy* 85 (5), 967–977. <http://dx.doi.org/10.1016/j.solener.2011.02.013>. ISSN 0038-092X.
- Mejia, J.F., Huntington, J., Hatchett, B., Koracin, D., 2012. Linking global climate models to an integrated hydrologic model using a hybrid downscaling approach. *J. Contemp. Water Res. Educ.* 147 (1), 17–27. <http://dx.doi.org/10.1111/j.1936-704X.2012.03100.x>.
- Mejia, J.F., Douglas, M.W., Lamb, P.J., 2016. Observational investigation of relationships between moisture surges and mesoscale- to large-scale convection during the North American monsoon. *Int. J. Climatol.* 36, 2555–2569. <http://dx.doi.org/10.1002/joc.4512>.
- Mejia, J.F., Douglas, Michael W., Lamb, Peter J., 2010. Aircraft observations of the 12–15 July 2004 moisture surge event during the North American monsoon experiment. *Mon. Weath. Rev.* 138, 3498–3513. <http://dx.doi.org/10.1175/2010MWR3228.1>.
- Mlawer, Eli J., Steven, J., Taubman, Patrick, Brown, D., Iacono, M.J., Clough, S.A., 1997. Radiative transfer for inhomogeneous atmospheres: RRTM, a validated correlated-k model for the longwave. *J. Geophys. Res.* 102, 16663–16682.
- Niu, G.-Yue., et al., 2011. The community Noah land surface model with multi-parameterization options (Noah-MP): 1. Model description and evaluation with local-scale measurements. *J. Geophys. Res.: Atmos.* 116, D12.
- Oakley, N.S., Redmond, K.T., 2014. A climatology of 500-hPa closed lows in the Northeastern Pacific Ocean, 1948–2011. *J. Appl. Meteorol. Climatol.* 53 (6), 1578–1592.
- Perez, Richard, Lorenz, Elke, Pelland, Sophie, Beauharnois, Mark, Van Knowe, Glenn, Hemker, Karl, Heinemann, Detlev, et al., 2013. Comparison of numerical weather prediction solar irradiance forecasts in the US, Canada and Europe. *Sol. Energy* 94, 305–326.
- Rasmussen, R., Liu, C., Ikeda, K., Gochis, D., Yates, D., Chen, F., Miller, K., et al., 2011. High-resolution coupled climate runoff simulations of seasonal snowfall over Colorado: a process study of current and warmer climate. *J. Clim.* 24 (12), 3015–3048.
- Reno, M., Hansen, C., Stein, J., 2012. Global Horizontal Irradiance Clear Sky Models: Implementation and Analysis, Sandia National Laboratories, SAND2012-2389.
- Roebber, P.J., 2010. Seeking consensus: a new approach. *Mon. Weather Rev.* 138 (12), 4402–4415.
- Rogers, P.J., Johnson, R.H., 2007. Analysis of the 13–14 July gulf surge event during the 2004 North American Monsoon Experiment. *Mon. Weather Rev.* 135 (9), 3098–3117.
- Ruiz-Arias, J.A., Dudhia, J., Santos-Alamillos, F.J., Pozo-Vázquez, D., 2013. Surface clear-sky shortwave radiative closure intercomparisons in the Weather Research and Forecasting model. *J. Geophys. Res. Atmos.* 118, 9901–9913. <http://dx.doi.org/10.1002/jgrd.50778>.
- Seastrand, S., Serra, Y., Castro, C., Ritchie, E., 2014. The dominant synoptic-scale modes of North American monsoon precipitation. *Int. J. Climatol.* <http://dx.doi.org/10.1002/joc.4104>.
- Sengupta, M., Habte, Aron, Kurtz, Sarah, Dobos, Aron, Wilbert, Stefan, et al., 2015. Best Practices Handbook for the Collection and Use of Solar Resource Data for Solar Energy Applications. [Research Report] Technical Report NREL/TP-5D00-63112, National Renewable Energy Laboratory, pp. 236.
- Sharma, N., Sharma, P., Irwin, D., Shenoy, P., 2011. Predicting solar generation from weather forecasts using machine learning. In: Smart Grid Communications (SmartGridComm). In: 2011 IEEE International Conference on, IEEE, pp. 528–533.
- Shedd, S., Hodge, B.M., Florida, A., Orwig, K., 2012. A statistical characterization of solar photovoltaic power variability at small timescales. In: 2nd Annual International Workshop on Integration of Solar Power into Power Systems Conference, Lisbon, Portugal (Nov 2012).
- Silverman, N.L., Maneta, M.P., Chen, S.-H., Harper, J.T., 2013. Dynamically downscaled winter precipitation over complex terrain of the Central Rockies of Western Montana, USA. *Water Resour. Res.* 49. <http://dx.doi.org/10.1029/2012WR012874>.
- Skamarock, W.C., Klemp, J.B., Dudhia, J., Gill, D.O., Barker, D.M., Duda, M.G., Huang, X.-Y., Wang, W., Power, J.G., 2008. A description of the Advanced Research WRF version 3 NCAR Tech Note NCAR/TN-475+STR, 2008, pp. 113. [Available from UCAR

- Communications, P. O. Box 3000, Boulder, CO 80307, J.
- Skamarock, William C., Klemp, Joseph B., 2008. A time-split nonhydrostatic atmospheric model for weather research and forecasting applications. *J. Comput. Phys.* 227 (7). <http://dx.doi.org/10.1016/j.jcp.2007.01.037>.
- Sperati, S., Alessandrini, Stefano, Monache, Luca Delle, 2016. An application of the ECMWF ensemble prediction system for short-term solar power forecasting. *Sol. Energy* 133, 437–450. <http://dx.doi.org/10.1016/j.solener.2016.04.016>. ISSN 0038-092X.
- Stensrud, D.J., 2009. *Parameterization Schemes: Keys to Understanding Numerical Weather Prediction Models*. Cambridge University Press.
- Thompson, Gregory., Field, Paul R., Rasmussen, Roy M., Hall, William D., 2008. Explicit forecasts of winter precipitation using an improved bulk microphysics scheme. Part II: implementation of a new snow parameterization. *Mon. Weather Rev.* 136, 5095–5115.
- Verzijlbergh, Remco A., Heijnen, Petra W., de Roode, Stephan R., Los, Alexander, Jonker, Harm J.J., 2015. Improved model output statistics of numerical weather prediction based irradiance forecasts for solar power applications. *Sol. Energy* 118, 634–645. <http://dx.doi.org/10.1016/j.solener.2015.06.005>. ISSN 0038-092X.
- Voyant, Cyril, Soubdhan, Ted, Lauret, Philippe, David, Mathieu, Muselli, Marc, 2015. Statistical parameters as a means to a priori assess the accuracy of solar forecasting models. *Energy* 90 (Part 1), 671–679. <http://dx.doi.org/10.1016/j.energy.2015.07.089>. ISSN 0360-5442.
- Walcek, C.J., 1994. Cloud cover and its relationship to relative humidity during a springtime midlatitude cyclone. *Mon. Weather Rev.* 122 (6), 1021–1035.
- Wilcox, Stephen, 2007. National Solar Radiation Database 1991–2005 Update: User's Manual. No. NREL/TP-581-41364. National Renewable Energy Laboratory (NREL), Golden CO.
- Wilks, D.S., 2011. *Statistical Methods in the Atmospheric Sciences*, third ed. Elsevier 676 pp.
- Zack, John, 2010. Current status and challenges of solar power production forecasting. In: Proc. ETWG Solar Workshop, Austin, TX, 2011.
- Zempila, M.M., Giannaros, T.M., Bais, A., Melas, D., Kazantzidis, A., 2016. Evaluation of WRF shortwave radiation parameterizations in predicting Global Horizontal Irradiance in Greece. *Renew. Energy* 86, 831–840. <http://dx.doi.org/10.1016/j.renene.2015.08.057>.
- Zhang, H., Pu, Z., Zhang, X., 2013a. Examination of errors in near-surface temperature and wind from WRF numerical simulations in regions of complex terrain. *Weather Forecast.* 28 (3), 893–914.
- Zhang, Jie, Hodge, Bri-Mathias, Florita, Anthony, Lu, Siyuan, Hamann, Hendrik F., Banunarayanan, Venkat, 2013. Metrics for evaluating the accuracy of solar power forecasting. In: 3rd International workshop on integration of solar power into power systems, London, England.